

Revealing Exciton Dynamics in a Small-Molecule Organic Semiconducting Film with Subdomain Transient Absorption Microscopy

Cathy Y. Wong,[†] Samuel B. Penwell,^{†,‡} Benjamin L. Cotts,^{†,‡} Rodrigo Noriega,[†] Hao Wu,[†] and Naomi S. Ginsberg^{*,†,‡,§,||}

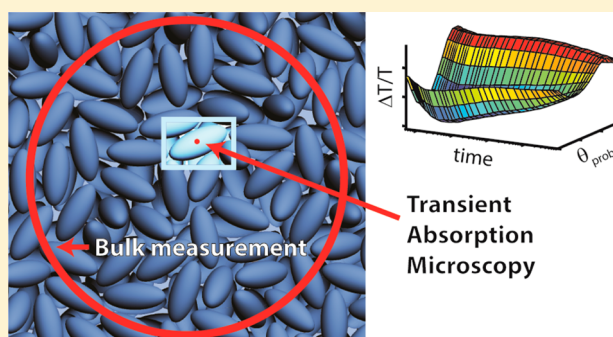
[†]Department of Chemistry and [‡]Department of Physics, University of California, Berkeley, California 94720, United States

[§]Physical Biosciences and Materials Sciences Division, Lawrence Berkeley National Laboratory, Berkeley, California 94720, United States

^{||}Kavli Energy NanoSciences Institute, Berkeley, California, 94720 United States

S Supporting Information

ABSTRACT: The ultrafast spectroscopy of single domains of polycrystalline films of TIPS-pentacene, a small-molecule organic semiconductor of interest in electronic and photovoltaic applications, is investigated using transient absorption microscopy. Individual domains are distinguished by their different polarization-dependent linear and nonlinear optical responses. As compared to bulk measurements, we show that the nonlinear response within a given domain can be tied more concretely to specific physical processes that transfer exciton populations between specified electronic states. By use of this approach and a simple kinetic model, the signatures of singlet fission as well as vibrational relaxation of the initially excited singlet state are identified. As such, observing exciton dynamics within and comparing exciton dynamics between different TIPS-pentacene domains reveal the relationship between photophysics and film morphology needed to improve device performance.



1. INTRODUCTION

Photovoltaic devices using organic semiconductors are particularly attractive as a solution for our increasing energy needs, as their material properties can be chemically tuned, and they are amenable to high-throughput production.^{1–5} However, the efficiency of organic photovoltaics (OPVs) is still low: the highest reported power conversion efficiency for a single junction organic solar cell is around 9%.⁶ In order to understand and improve the efficiency of these devices, we must understand the fate of the photogenerated exciton. The steps in OPV device function are photogeneration of excitons, exciton migration to a donor–acceptor interface, charge separation, and migration of the charges to an electrode. The fate of the exciton immediately after photogeneration can be monitored using pulsed laser techniques such as transient absorption (TA) spectroscopy,^{7–13} whereby a “pump” pulse excites the sample, and after a controlled time delay, a “probe” pulse records the resulting evolution of the exciton.

Many promising organic semiconducting materials tend to form films with a complex microstructure that can impact device functionality.^{14–19} Two major classes of these materials are polymer-based and small-molecule-based organic semiconductors, both of which possess varied microstructures. Polymer-based films are comparatively disordered, with small characteristic morphological length scales,^{20–25} while small-

molecule based films can possess longer-range order.^{17,26–29} Regular alignment of these small molecules within each domain enhances exciton and charge diffusion, improving device performance.^{26,30} However, a typical TA experiment uses mirrors or lenses which focus the pump and probe beams to a 100–1000 μm diameter beam waist at the sample position. When the sample has a microstructure that is smaller than this length scale, such a TA measurement necessarily averages over different microstructural features, obscuring the dynamics.

The relationship between excitation dynamics and microstructure in organic thin films can be investigated by reducing the extent of the optical focal spot used to perform a TA measurement—in other words, by performing TA microscopy. TA microscopy is particularly well-suited to examining small-molecule thin films because the characteristic length scales over which order exists can be larger than the optical diffraction limit, opening up the possibility to interrogate individual homogeneous domains rather than averaging over a series of them. A similar approach has previously been realized to provide a contrast agent with molecular specificity in biological imaging^{31–35} and also to understand spatial heterogeneity in

Received: July 31, 2013

Revised: October 3, 2013

Published: October 15, 2013

the excited-state dynamics of inorganic nanostructures,^{36–43} graphene,^{44–47} perylene microcrystals,^{48–50} and OPV polymer blends.^{51–55}

Films of small-molecule polyacenes, which form crystalline domains, have been studied since the 1940s as model systems, without much mention of their potential for practical usage.^{56–60} However, their strong π -stacking, absorption in the visible wavelength region, ability to form well-ordered molecular crystals, large carrier mobilities, and ability to undergo singlet fission have recently been identified as being well suited for use in optoelectronic devices, driving a resurgence of research activity.^{10,26,61–68} The properties of these polyacenes can be tuned by the chemical functionalization of their structure. For example, in 6,13-bis-(triisopropylsilyl)ethynyl-pentacene (TIPS-Pn), shown in Figure 1a, the bulky side groups allow the molecule to be soluble in organic solvents for solution processing. They also change the packing structure of the molecular crystal, decreasing the π -stacking distance,^{69–71} leading to an increase in carrier mobility, and stability in air. Additionally, under certain conditions, TIPS-Pn can pack in large 100- μ m-wide

domains in solution-processed films, while still retaining the properties of pentacene that make it attractive for use in organic electronic devices.^{72,73}

Previous TA studies on TIPS-Pn have used excitation spot sizes greater than 200 μ m in diameter, and as such represent bulk measurements.^{10,74–76} In this work, by reducing the spot size area by ~ 1000 times to a diameter of 8 μ m, we perform TA microscopy on films of TIPS-Pn, allowing us to interrogate areas much smaller than the size of a typical domain, providing insight that is unavailable in bulk TA measurements. Since there do not appear to be drastic changes in orientation of TIPS-Pn molecules within our excitation volume, it is possible to study the effect of varying the incident probe polarization. This polarization-dependent TA data, unavailable in a bulk measurement that averages over multiple grains, plays a pivotal role in determining the origin of the observed exciton dynamics. It enables us to distinguish three features in the data that represent the evolution of excited-state populations, which we assign to ultrafast exciton thermalization, singlet fission, and exciton recombination. It also enables us to compare the optical signatures from different domains. These insights into the relationship between the electronic and the physical structure of films could aid in better understanding device performance.

2. EXPERIMENTAL SECTION

2.1. Film Preparation and Characterization. Glass substrates were sonicated for 10 min in acetone, soapy water, and then isopropyl alcohol with rinses of that solvent between each step. During deposition the substrates were placed onto an aluminum block on top of a hot plate held between 60 and 70 $^{\circ}$ C. Approximately 40 μ L of filtered (0.2 μ m pore size) 5 mg/mL TIPS-Pn in toluene solution was drop cast onto the substrates and immediately covered with a 100 mm Petri dish to control the evaporation rate. This yielded 600 nm thick films with fingerlike domains 50–150 μ m wide and multiple millimeters long (Figure 1b).

Optical profilometry measurements were taken on an ADE MicroXAM-100 optical profilometer. Crosses were scribed into the sample to delineate regions of interest and to provide a zero for the thickness measurements. Linear absorption measurements were taken on a Cary 100 UV–vis spectrophotometer (Figure 1c). Samples were then mounted face down onto large rectangular coverslips for TA measurements.

2.2. Transient Absorption Microscopy. TA microscopy measurements were conducted in a home-built optical microscope (Figure 2). Briefly, an 80 MHz mode-locked Ti:sapphire Coherent Mantis oscillator was used to seed a 5 kHz Coherent Legend-Elite regenerative amplifier. This pumped an optical parametric amplifier (Coherent OPeA Solo) to produce laser light centered at 700 nm (Figure 1c), pumping the $S_0 \rightarrow S_1$ transition of TIPS-Pn. The beam was then split into degenerate pump and probe pulses in a 4:1 intensity ratio that were fed into a 0.4 NA 10X Plan Apo Leica objective to yield sub-10- μ m-diameter spot sizes (fit to $1/e^2$) with pulse duration of ~ 35 fs (fwhm). As shown in Figure 2, the collinearly propagating pulses were offset equidistant from the optical axis of the objective so that they would focus to the same spot in the sample plane. Energy fluences were set relatively low to avoid sample photodamage (400 μ J/cm² for pump; 100 μ J/cm² for probe) as confirmed by a power dependence study (Figure S3 in the Supporting Information). Power was set for the pump and probe beams through separate

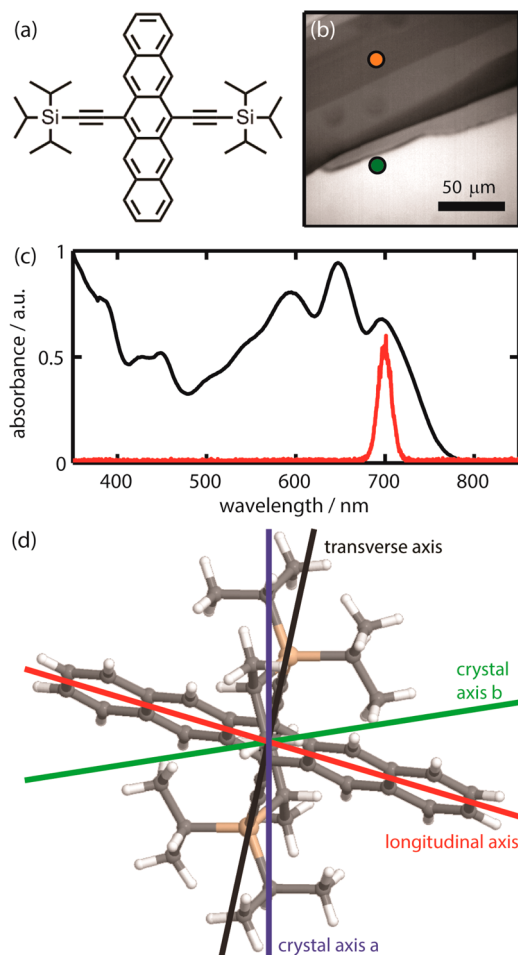


Figure 1. (a) Chemical structure of TIPS-Pn. (b) Linear transmission image of a TIPS-Pn film. Orange and green spots denote locations where data is discussed in the text. (c) Bulk linear absorption spectrum of TIPS-Pn film (black) and spectrum of the pump and probe pulses (red). (d) Orientation of a TIPS-Pn molecule in a film, where the plane formed by crystal axes *a* and *b* is parallel to the sample plane and is shown here as parallel to the page.

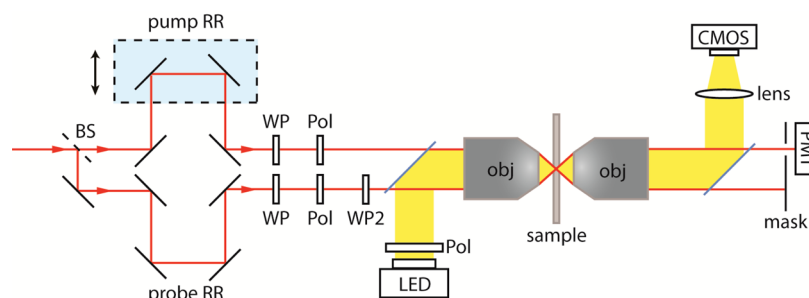


Figure 2. Schematic of transient absorption microscope. BS = 50:50 beam splitter, RR = retroreflector, WP = waveplate, Pol = polarizer, obj = 0.4 NA 10 \times objective. Solid blue lines represent removable mirrors for laser/LED illumination and detecting with PMT/CMOS camera.

waveplate and polarizer combinations. Additionally, probe polarizations were varied in steps of 15 degrees from 0°–180° by rotating a second waveplate (Figure 2). After passing through the sample, the transmitted beams were collected using an identical objective to the first, and the pump beam was removed via spatial filtering while the probe signal was focused onto a Hamamatsu H9306-03 photomultiplier tube (PMT). The output from the PMT was split and coupled to two lock-in amplifiers, with one locked to the pump chopping frequency (500 Hz) to collect the unnormalized TA signal, ΔT , and the other locked to the laser pulse repetition rate to collect the probe transmission signal, T . By rastering the sample position using a computer-controlled Physik Instrumente piezostage, spatial maps of $\Delta T/T$ were generated. Additionally, by toggling the kinematically mounted mirrors shown in blue in Figure 2, the beam path could be modified to focus onto a CMOS camera (Thorlabs DCC1545M) for imaging the beams or sample.

3. RESULTS

Transient absorption microscopy enables the domain-specific interrogation of excited-state population evolution, and operates on the same general principles as bulk TA measurements, with the added enhancement of spatial resolution. TA operates by focusing two laser pulses, one pump and one probe, onto the same spatial location on a sample and by varying the time delay between the arrival of each pulse. The small change ΔT in the amount of transmitted probe light as a result of pump excitation is measured as a function of this time delay. It is thus possible to quantify the excited-state dynamics of the sample since the change in probe transmission is completely dependent on the instantaneous population distribution in the probed sample volume. The TA signal normalized by the amount of transmitted probe light, referred to as $\Delta T/T$, allows for global comparisons of data, since this quantity is proportional to the differential optical density experienced by the probe as a result of prior pump excitation. This signal can be positive or negative, depending on whether, when the probe pulse arrives, the sample is more or less absorptive than it would be in its ground state. Probe absorption on a transition between two excited states (excited-state absorption, or ESA) is negative, while positive signals arise from ground-state bleaching (GSB) and stimulated emission (SE). Analysis of the magnitudes of these signal components and of their evolution in time can yield insight into the population dynamics and electronic structure of the system.

Implementing TA with spatial resolution permits measurements of the excited-state dynamics specific to a given, smaller homogeneous region within a heterogeneous sample. While it

is possible that heterogeneity exists below the size of the 8 μm diameter beam in these experiments, the clear contrast in the polarization dependence of the resulting signals indicates that the examined areas are highly anisotropic in their structure, suggesting a high degree of crystallinity. While smaller excitation spot sizes can be achieved (by using objectives with higher numerical aperture or by overfilling the objective and using different wavelengths for pump and probe), they increase the data scan time and were not necessary for the polycrystalline sample studied in this work. Note that the packing structure of TIPS-Pn molecules in a film deposited on a substrate is different from that of single crystals formed by growth in a solvent.^{69,77} While a bulk TA measurement might suffice for a single crystal, TA microscopy is needed to measure individual domains in TIPS-Pn films, which are of practical relevance for potential devices.

The multiple advantages of using a smaller excitation volume to probe thin films are demonstrated in Figure 3, which shows TA microscopy images of the same region of interest of a TIPS-Pn film as in Figure 1b, each obtained with a fixed pump–probe time delay τ and fixed laser pulse polarizations. The left-hand column displays images measured after a very brief 50 fs of time evolution, and the right-hand column displays images measured after 500 ps. The pump pulse, tuned to the S_0 – S_1 transition at the band edge (Figure 1c), generates an excited S_1 population proportional to the projection of the pump field onto the S_0 – S_1 transition dipole moment. As there is only one resonant transition from the ground state, varying the pump polarization serves only to vary the size of the excited-state population prepared in S_1 . Therefore, we hold the pump polarization fixed, to initiate the exciton dynamics with the same initial S_1 population in all measurements. After a delay, this initially prepared population can redistribute among various excitonic states so that the probe pulse may couple additional states (e.g., in ESA transitions), instead of only the S_0 – S_1 transition resonant with the pump pulse. Since each of these transitions may have different transition dipole moment orientations, varying the polarization of the probe field while holding the pump polarization fixed allows us to better decouple the optical response of the probe from the exciton dynamics.

By considering the various images in Figure 3, it is evident that TA can furthermore be used as a contrast agent to discern TIPS-Pn domains. Different combinations of laser pulse polarizations readily reveal that each domain has its own well-defined orientation and accompanying transition dipole moments. Specifically, each panel has been measured with the pump pulse polarized at 45°, and with the probe polarization θ_{pr} stepped from top to bottom of the figure in 45° increments. The false color of the images represents the sign and magnitude

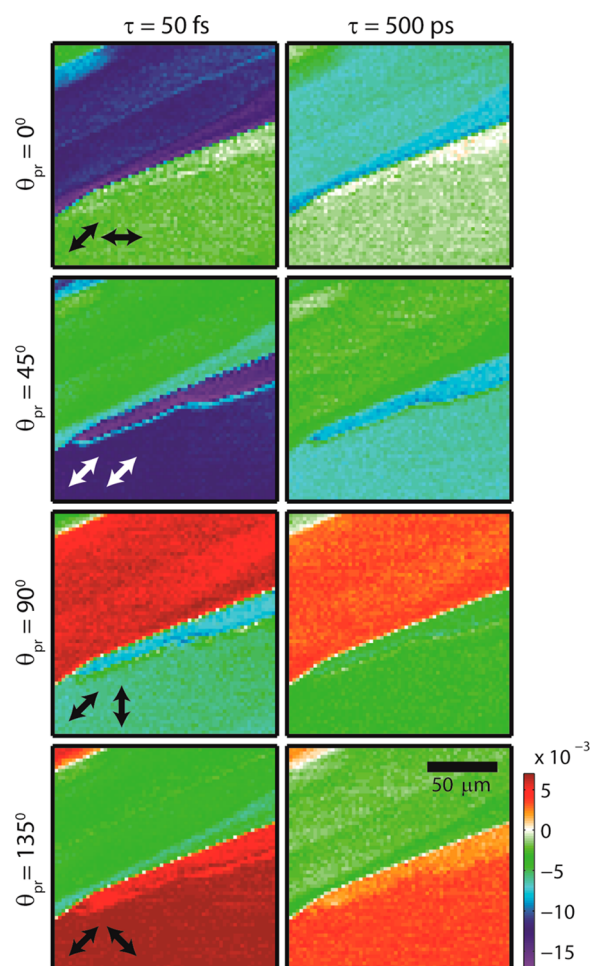


Figure 3. TA images of the TIPS-Pn film shown in Figure 1b at four probe polarizations ($\theta_{\text{pr}} = 0^\circ, 45^\circ, 90^\circ, 135^\circ$) and two population delay times ($\tau = 50$ fs, 500 ps). Arrows indicate the polarization of the pump and probe pulses ($\theta_{\text{pump}} = 45^\circ$; pump fluence = $400 \mu\text{J}/\text{cm}^2$; probe fluence = $100 \mu\text{J}/\text{cm}^2$ for all measurements).

of the TA signal, with positive, red tones indicating that SE or GSB dominates, and with negative, green and blue tones indicating progressively stronger ESA. Abrupt changes in color as a function of position therefore indicate boundaries between domains, most noticeably the boundary between the large upper domain and the large lower domain within the imaged region of the film. (A small region of another domain is also evident in the top left corner.) For example, the lower domain has a strong positive (red) TA signal when the probe is polarized at $\theta_{\text{pr}} = 135^\circ$ and a strong negative TA signal when the probe is polarized at $\theta_{\text{pr}} = 45^\circ$. This polarization dependence is shifted for the upper domain, which has the strongest positive TA signal at $\theta_{\text{pr}} = 90^\circ$ and a negative TA signal at $\theta_{\text{pr}} = 0^\circ$. In contrast, in a bulk TA measurement, where many domains in various orientations are averaged together, the signal obtained at each probe polarization would appear homogeneous—it would be an average of all of the polarization-specific signals that we measure. The entire multidimensional result of Figure 3 would then be reduced to two values: a single TA signal value at $\tau = 50$ fs and another at $\tau = 500$ ps. By reducing the excitation volume in TA microscopy, we can determine the relationship between the polarization-dependent TA signal and the relative molecular orientation within each domain.

The TA signals collected at two particular locations in the film are presented in more detail in Figure 4. Panels a, c, and e show data collected from a particular location in the upper domain, labeled by the orange dot in Figure 1b, while panels b, d, and f show data collected from a spot in the lower domain, indicated in Figure 1b in green.

The surfaces in panels a and b show the TA signal as a function of delay time and probe polarization at these two film locations. Note that the zero signal level is close to the top of these plots, indicating that ESA can overall be much stronger than the SE and GSB contributions to the TA signal. The different weights of ESA and of SE or GSB depend on which transitions are coupled most strongly to a given probe polarization. For example, the transition dipole moments along the long and short axes of the pentacene in Figure 1d are roughly orthogonal in the sample plane and correspond respectively to S_1 ESA and to S_0 – S_1 transitions, as elaborated in the Discussion section. At both locations, a periodic dependence of the TA signal on probe polarization is observed, but the phases of these oscillations are different, reflecting the different orientations of the two domains. This is more clearly shown in panels c and d where the blue curves (filled circles) show slices of the surfaces in panels a and b, respectively, at $\tau = 1$ ps. While both curves clearly show the periodic dependence of the TA signal on probe pulse polarization, the lower domain (green spot) has a maximal positive TA signal at $\theta_{\text{pr}} \sim 140^\circ$ while the upper domain has a maximal positive TA signal at $\theta_{\text{pr}} = 90^\circ$. The red curves (unfilled circles) in these same plots show the polarization dependence of the linear transmission. These curves are also periodic, but are almost exactly out of phase with the polarization dependence of their corresponding TA signals. These polarization trends are common in the films of TIPS-Pn that we have measured and are useful in determining which excited states are being populated in the ultrafast dynamics that follow pump excitation, as discussed in more detail below.

By inspection of the surfaces of panels a and b in Figure 4, the population dynamics at the two film locations can be revealed. Regardless of whether the TA signal is initially positive or negative, at each probe polarization, $\Delta T/T$ initially decreases and subsequently increases as a function of time. Then, at later times, the magnitude, $|\Delta T/T|$, decays toward zero, irrespective of sign. This is more clearly observed in panels e and f of Figure 4, which show transients at various polarizations collected respectively at the orange location in the upper domain and at the green location in the lower domain in Figure 1b. The black curves in Figure 4e,f show fits of the TA signal at each polarization, using a triexponential with a constant offset, $y = a_1 \exp(-x/t_1) + a_2 \exp(-x/t_2) + a_3 \exp(-x/t_3) + c$. A full set of transients and fits for both film locations can be found in Figure S1, the fit parameters can be found in Table S1 and Table S2, and plots of fit parameters as a function of probe polarization are shown in Figure S2, all in the Supporting Information. For each of the incident probe polarizations, the time constants are ~ 50 fs, 3 ps, and 250 ps. As expected, the time constants for the three exponentials do not show a strong probe polarization dependence because these time constants are tied to the material-specific evolution of excited-state population distribution that occurs up to the instant before probe interrogation. In contrast, the amplitudes of the three exponentials are dictated by the light–matter interaction of the probe with the instantaneous population distribution of the system at each time delay and thereby are

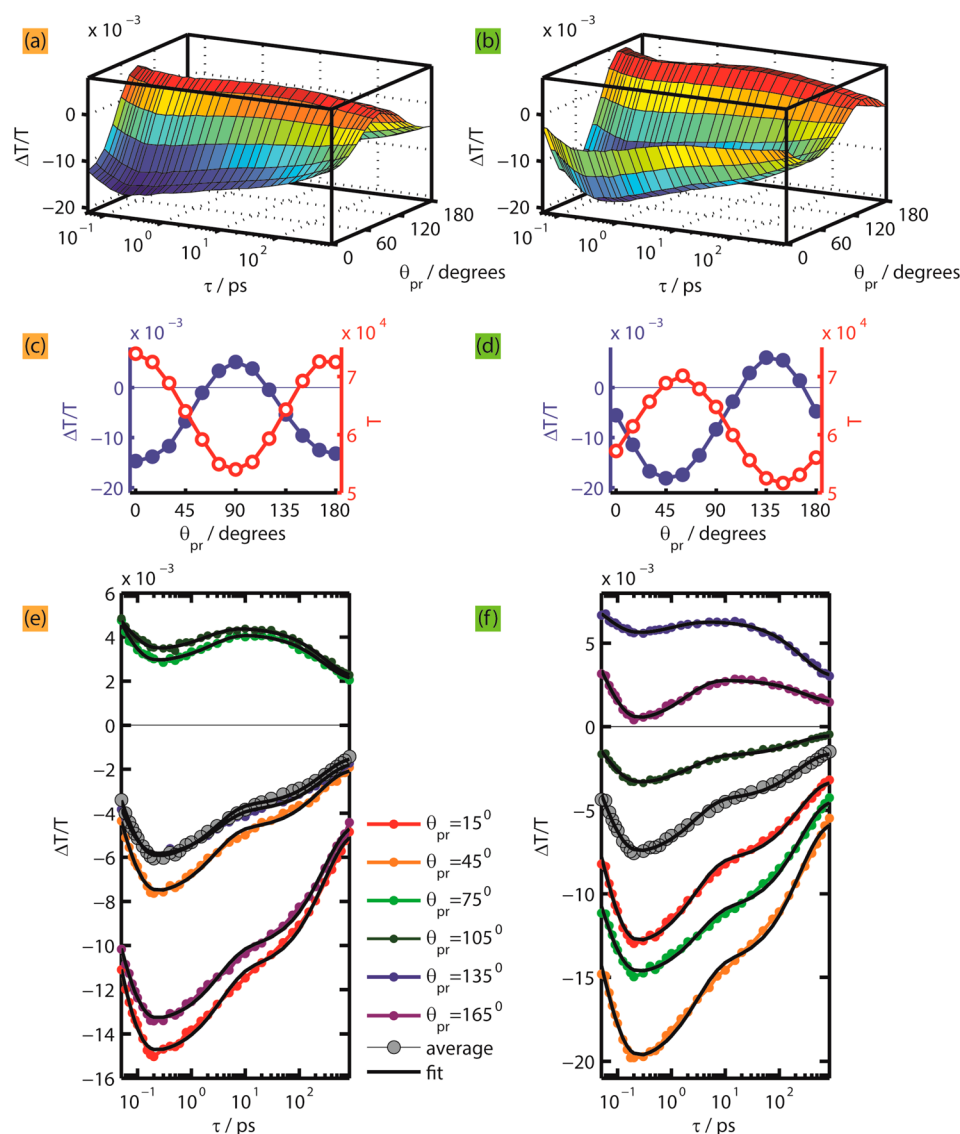


Figure 4. TA signal collected at the (a,c,e) orange and (b,d,f) green locations shown in Figure 1b. (a,b) TA signal as a function of delay time and probe polarization. (c,d) Dependence of TA signal (blue, filled circles) and probe transmission (red, unfilled circles) on probe polarization, at $\tau = 1$ ps. Lines are interpolations between data points. (e,f) TA signal dynamics collected using various probe polarizations, the average of the data collected at all polarizations (gray), and fits of each transient to a triexponential. ($\theta_{\text{pump}} = 45^\circ$; pump fluence = $400 \mu\text{J}/\text{cm}^2$; probe fluence = $100 \mu\text{J}/\text{cm}^2$ for all measurements).

strongly dependent upon probe pulse polarization. In addition to separating the probe response from the exciton dynamics, a major utility of probe-polarization-dependent TA measurements is that the results can distinguish between excited-state population transfer and exciton relaxation to the ground state. While exciton relaxation results in a signal whose magnitude decays in time irrespective of sign, the excited-state population transfer processes result in uniformly increasing or decreasing $\Delta T/T$ over time, irrespective of the probe pulse polarization and hence irrespective of the initial sign of the signal. This pattern is only rendered obvious by polarized interrogation at the single domain level. By contrast, a bulk measurement of many differently oriented domains would be analogous to the average of the TA signal at each of the different probe polarizations, shown in gray circles in Figure 4e,f, which would not allow the patterns in the exponential amplitudes to assist in the assignments described in the Discussion section below. Furthermore, while the magnitudes that we obtain for

exponential components of the transients at the two sample locations are quite different (Figure S2 in the Supporting Information), our analysis reveals that their time constants are similar, and the polarization information enables us to reconcile the kinetics at the two different spots.

4. DISCUSSION

Our approach of focusing on the exciton dynamics within individual domains of TIPS-Pn films enables more specific information to be collected in order to tease out the complex relationship between the physical structure and the electronic structure of a film and its dynamics. Below, we focus our remarks on the time and polarization dependence of the data described above for the green spot in the lower domain in the region of interest in Figure 1b. Using this spot as a case study, we are able to infer which processes can be responsible for the measured time components, and we are able to construct a kinetic model that is consistent for both the orange and green

spots, even though they are in different domains. Together, our analysis and modeling provide insight into structure–function relationships in TIPS-Pn films that would be far more difficult to achieve through bulk measurement alone.

Before proceeding to characterize the data, it is necessary to understand the geometry of pertinent transition dipole moments with respect to the TIPS-Pn crystal structure and orientation in order to identify populated excited states that can contribute to ESA. Since ESA is stronger than GSB and/or SE in this sample, when the TA signal is maximally positive, the probe field likely has the weakest coupling to any ESA transitions. As shown in both panels c and d of Figure 4, the polarization that results in the strongest positive TA signal (blue peak) closely corresponds to the polarization with the smallest linear transmission (red trough), or the highest linear absorption. Thus, we observe that when the field is optimally coupled to the transition dipole moment of the initial pump excitation transition, $S_0 \rightarrow S_1$, any ESA contributions are minimized due to weaker coupling. Additionally, the maximum ESA signal occurs at a probe polarization that is orthogonal to the pump's maximum absorption. We deduce that the transition dipole moments for these two transitions, $S_0 \rightarrow S_1$ and $S_1 \rightarrow S_n$ (for some higher-lying singlet state, S_n), are likely orthogonal to one another when projected onto the sample plane.

The common orientation of a TIPS-Pn molecule within a film with respect to the substrate, as measured by X-ray diffraction,⁷⁷ is illustrated in Figure 1d, where the molecule has been rotated such that the a – b plane of the crystal, which is parallel to the substrate, is in the plane of the page. Thus, the axes shown in Figure 1d are projections onto the sample plane. It is well-known that the transition dipole moment between the ground state and S_1 is aligned along the short, or transverse, axis of the pentacene core of TIPS-Pn⁷⁸ (Figure 1d). From our observations, it is likely that the transition from S_1 to a higher energy S_n state has a transition dipole aligned along the long, or longitudinal, axis of the pentacene core. Based on the reported crystal structure of TIPS-Pn films,⁷⁷ the projections of the transverse and longitudinal axes of the TIPS-Pn molecule should be close to orthogonal in our microscope sample plane, as illustrated in Figure 1d. Minor variations in this packing structure would result in changes in the angle between these two projected transition dipoles, resulting in TA and transmission polarization dependence curves that do not exhibit the near-perfect anticorrelation shown in Figure 4d. We have measured a smaller subset of domains for which the dependence of the TA signal on probe polarization deviates to an even greater extent than the example shown in Figure 4d, implying that some regions of the film may have very different orientations, crystal textures, or overlapping domains. Nevertheless, we restrict our in-depth analysis to the representative data presented in Figure 4 and use the polarization dependence of T and $\Delta T/T$ to inform our assignment of the time components obtained from these data.

Three distinguishable exponential time components comprise the TA signal collected at both orange and green locations and at all measured polarizations: an ultrafast (~ 50 fs) exponential component with positive amplitude, a ~ 3 ps component with negative amplitude, and a slower ~ 250 ps decay toward zero that can have either positive or negative amplitude, depending on the probe pulse polarization (see Table S1 in the Supporting Information). While the comparison of these triexponential results to those of a bulk

TA study of TIPS-Pn films¹⁰ is made difficult by differing pump and probe wavelengths, by the longer instrument response function (150 fs) used in the bulk study, and by the smaller time range (850 ps) of the current work, we compare our findings to bulk TA measurements below. A previous fluorescence lifetime study of TIPS-Pn films had a time resolution of ~ 200 ps, and thus would be unable to resolve even the ~ 250 ps decay component reported here.⁷⁹

We assign the slow ~ 250 ps component that can be either positive or negative in amplitude to exciton recombination because it indicates that the excited-state population is simply being reduced during the evolution of the system. Note that this ~ 250 ps process has a fundamentally different polarization-dependent behavior than the behavior of the two faster 50 fs and 3 ps exponential time components, whose amplitudes remain consistently positive and negative, respectively, irrespective of probe polarization. These distinguishing characteristics form the foundation of our analysis and interpretation of the processes dictating population evolution at short times.

Consider first the fastest, ~ 50 fs component. The data that we present here are the first to report dynamics on this time scale in TIPS-Pn, as previous studies have had a longer instrument response function (150 fs). As discussed above, the decrease in the TA signal indicates an increase in probe absorption. This suggests that the exciton population evolves from its initially prepared state to a different state which has a stronger ESA or a weaker bleach than the initial state, with a time constant of ~ 50 fs. There are a number of possible states that could become populated on an ultrafast time scale—in particular, a vibrationally relaxed, or “thermalized,” S_1 state from which recombination could occur, a charge-separated state, or a higher-energy excitonic state as a result of singlet–singlet annihilation.^{80,81}

Curves showing the dependence of the TA signal on probe polarization, similar to those in Figure 4c,d, were plotted at a series of different delay times. Each curve was fit to a cosine-squared function, reflecting the dipole–field interactions, and we find that the phase of the polarization dependence does not change dramatically as a function of delay time (Figure S4 in the Supporting Information). We observe only a likely negligible shift of $\sim 2^\circ$. This shows that the physical processes that occur after the initial pump excitation do not result in a significant excited population in states that have a substantially different ESA transition dipole moment orientation than the absorptive transition dipole moment from the originally excited S_1 state.

In this regard, the simplest and most compelling possibility for the ultrafast process observed is that after initial excitation to a “hot” S_1 state, there is ultrafast thermalization into a lower energy S_1 state. If the thermalized S_1 state has a stronger transition dipole moment to or resonant transition with a higher excited state than the hot S_1 state, this process could cause the growth of the negative signal observed. This negative contribution would be stronger when the probe polarization is better aligned to the ESA transition dipole, as we observe. Vibrational relaxation from a hot to thermalized S_1 state would not likely change the orientation of the ESA transition dipole significantly, which also agrees with our measurements. Since the polarization dependence of the ESA does not change dramatically during this ~ 50 fs process, it is likely that the process does not involve two distinct electronic states, as it would be unlikely that they would have identical ESA transition

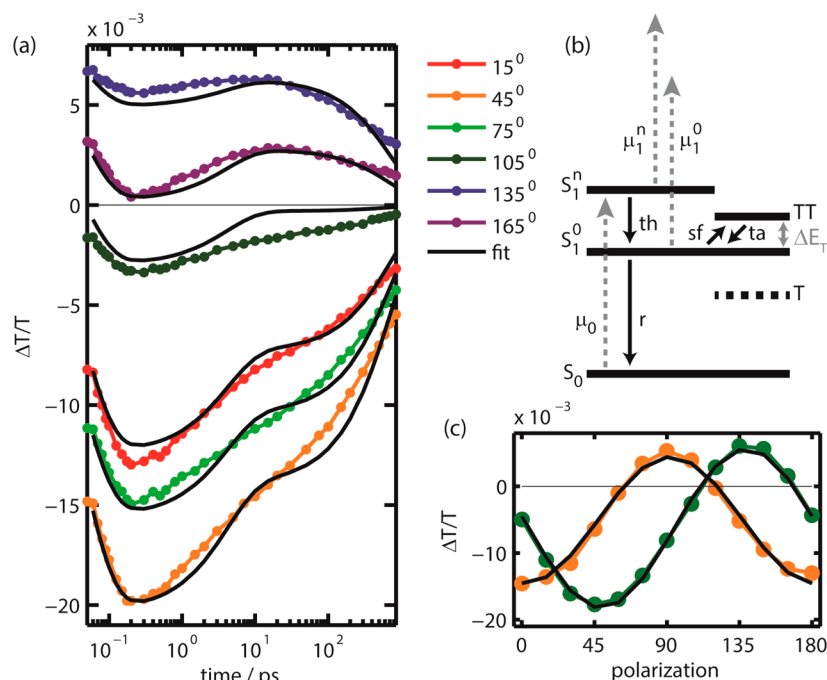


Figure 5. (a) TA signal as a function of time, collected at the “green” spot of Figure 1b at various polarizations and fits to the kinetic model in black. (b) Kinetic model, which includes four states (thick lines), rate constants (black arrows) and transition dipole moment strengths (dashed gray arrows). (c) TA signal at $\tau = 100$ fs as a function of polarization, collected at the “green” and “orange” spots of Figure 1b (circles), and fits to the kinetic model (black lines). ($\theta_{\text{pump}} = 45^\circ$; pump fluence = $400 \mu\text{J}/\text{cm}^2$; probe fluence = $100 \mu\text{J}/\text{cm}^2$ for all measurements.)

dipole moment orientations. Instead, the process is most simply explained as a transfer between two vibrational states of the same electronic state. This kind of relaxation could conceivably occur with the ultrafast rate constants observed in our measurements. Additionally, it is unlikely that spin flips would be able to occur on a time scale as fast as 50 fs, precluding intersystem crossing to triplet states and further suggesting that we observe internal conversion or vibrational relaxation.

Another possibility to explain the 50 fs time component is the creation of free carriers, either directly from the optical pump pulse or in a transition from the initially excited S_1 state.^{82–89} Terahertz measurements on TIPS-Pn have shown that an optical pump can create free carriers within 100 fs.^{74–76} It is possible that an ultrafast component in our TA signal could be the result of initially prepared S_1 excitons becoming free carriers. However, ESA from a free carrier would likely have a transition dipole moment that does not point specifically along the longitudinal pentacene axis. Instead it might point along the crystal axis with highest charge mobility. In the case of TIPS-Pn, this axis is the b axis of the crystal. According to the reported crystal structure for TIPS-Pn films,⁷⁷ the projections of the b axis illustrated in Figure 1d and of the S_1 transition dipole moment are 68° apart. This would not result in the polarization dependence curves shown in Figure 4c,d. Also, if the ultrafast 50 fs component were, indeed, indicative that S_1 population could convert to free carrier states, one would expect that the dependence of the TA signal on polarization would change dramatically within that time scale. This analysis does not preclude the possibility that free carriers are generated—it merely notes that free carriers are likely not the source of the 50 fs component observed in our signal.

At higher energy fluences, singlet–singlet annihilation could result in the population of a high energy exciton state or charge

separated state.^{81,80,90} However, power dependence measurements (see Figure S3 in the Supporting Information) show that, at the $\sim 400 \mu\text{J}/\text{cm}^2$ fluence used in this work, the TA signal is still in the linear regime. This precludes singlet–singlet annihilation from being a significant effect. Of the three main possibilities considered to explain the 50 fs time component, thermalization of a hot state, therefore, seems most likely.

Next, consider the possible physical meaning of the ~ 3 ps time component in the TA signal. This exponential component has a negative amplitude at all polarizations, meaning that the system has evolved such that after 3 ps there is either more GSB or more SE or less ESA. Two possible types of states often considered in similar organic semiconducting films that may satisfy this criterion are triplet states and trap states. In the solid state, TIPS-Pn is known to demonstrate singlet fission, whereby a single singlet excitation converts to a pair of occupied triplet states, each with approximately half the singlet energy.^{10,91} The reported absorption spectrum of the triplet state of TIPS-Pn films shows that no transition from the triplet state is resonant with our 700 nm probe pulse.¹⁰ Therefore, if the probe interacts with the system when a triplet state population has accumulated, the TA signal will reflect less ESA than otherwise. Furthermore, singlet fission produces two triplets from one singlet. This increases the corresponding amount of GSB signal. While less is known about trap states, it is possible that a trapped exciton is also not resonant with an ESA transition at 700 nm, reducing the amount of ESA signal. Further studies will be required to determine the nature and significance of these potential trap states. At present, however, the 3 ps time component seems most attributable to singlet fission. Although a direct comparison to the bulk TA study of TIPS-Pn films¹⁰ is not possible owing to the use of different pump and probe wavelengths, the bulk study did ascribe a 1.0 ps time constant to the rise of a triplet population formed by singlet fission,

which is slightly faster than the rate reported here. The small discrepancy may be owing to differing film morphologies or to the inclusion of TA signals from domain boundaries and film defects in the bulk measurement.

Based on the above analysis, the simplest explanation of the exciton dynamics in TIPS-Pn films involves initial excitation to a “hot” S_1 state at 700 nm that leads to ultrafast thermalization, followed by the possibility of relatively rapid singlet fission and a much slower time scale exciton recombination. On the basis of this analysis, we fit transients to the dynamics of a four-level kinetic model (Figure S5a,b). We included hot and relaxed singlet excited states, S_1^h and S_1^o , and a doubly occupied triplet state, TT, in addition to the ground state, S_0 . (The energy of a single triplet excitation is indicated with a dashed line.) These states are coupled to one another as follows: k_{th} represents the $S_1^h \rightarrow S_1^o$ thermalization rate, k_{sf} is the rate of singlet fission ($S_1^o \rightarrow TT$), the reverse process of triplet pair annihilation is included with a rate k_{ta} , and finally the rate of internal conversion from S_1^o to S_0 is given by k_r . The coupled differential equations describing the rate laws that govern the population dynamics of the excited states can be summarized in matrix form as

$$\frac{d\mathbf{S}}{dt} = \mathbf{KS}$$

where $\mathbf{S} = \mathbf{S}(t) = [S_1^h(t); S_1^o(t); TT(t)]$ is a column vector of the excited-state populations at a given time t with an initial condition $\mathbf{S}_i = [1; 0; 0]$, and \mathbf{K} is the matrix of rate constants coupling the states

$$\mathbf{K} = \begin{bmatrix} -k_{th} & 0 & 0 \\ k_{th} & -(k_{sf} + k_r) & k_{ta} \\ 0 & k_{sf} & -k_{ta} \end{bmatrix}$$

In order to enable the fit to address parameters which are more physically significant, the equilibrium rate constant for the rise time of the triplets, $k_T = k_{sf} + k_{ta}$, and the energy gap between the TT and S_1^o state, $\Delta E_T = E_{TT} - E_{S_1^o}$, are optimized, while ensuring detailed balance (see Supporting Information for details).

Solving these coupled differential equations gives the time-dependent population of each excited state. The TA signal, as a function of time delay and probe polarization, may then be calculated as (see Supporting Information for details)

$$\frac{\Delta T}{T}(t, \theta) = A_0(\theta)S_V(t) - A_1^o(\theta)S_1^o(t) + [A_0(\theta) - A_1^h(\theta)]S_1^h(t)$$

where S_V is the number of ground-state vacancies, and the amplitudes A_0 , A_1^o , and A_1^h include the couplings of the probe field with the transition dipoles μ_0 , μ_1^o , and μ_1^h , respectively. The first dipole, μ_0 , is for transitions between S_0 and S_1^h . This dipole generates GSB and SE signals. The other two, μ_1^o and μ_1^h , are ESA dipoles, which corresponds to absorption from S_1^o and S_1^h , respectively, to higher lying levels. Absorption from the triplet state is neglected, as there is no transition from this level that is resonant with our 700 nm laser pulse.¹⁰

A trust-region-reflective algorithm was used to perform a simultaneous least-squares fit of the simulated signal to the TA data for the entire set of time points and at a set of 13 probe polarizations, with $[k_{th}, k_T, \Delta E_T, k_r, A_0, A_1^o, A_1^h]$ as fitting

parameters, and A_0 , A_1^o , and A_1^h obeying the functional form $a + b \cos^2(\theta + c)$. Data from both positions on the sample (described previously as the orange and green spots in Figure 1b) were used in a global fitting routine, where both data sets were fit simultaneously. The fitting parameters for the rate constants and excited-state dipole moments were independent for each sample position, with the only constraint being their S_0 to S_1 transition dipole (μ_0). The orientation of μ_0 for each domain is taken from the polarization-dependent transmission curves in Figure 4c,d. Additionally, the ratio of the amplitude of this dipole moment can be inferred from the modulation of the linear transmission. The orientations of A_1^o and A_1^h are set to remain parallel to each other, but are otherwise free to have any orientation in each domain. The rates and energy splitting have no dependence on polarization, but are allowed to take independent values in each domain.

The resulting fit to the transients taken at the green spot is shown in Figure 5a. Additional polarization traces and the fit to data from the orange spot are shown in Figure S5 in the Supporting Information, a table of the resulting rate constants can be found in Table 1, and the calculated amplitudes A_0 , A_1^o ,

Table 1. Parameters Extracted by Fitting TA Signal to the Kinetic Model

	$1/k_{th}$ (fs)	$1/k_T$ (ps)	ΔE_T (meV)	$1/k_r$ (ps)	A	fits
green spot	45	4.2	26	555	Figure S6a	Figure S5a,b
orange spot	43	4.7	26	665	Figure S6b	Figure S5c,d

and A_1^h are shown in Figure S6 in the Supporting Information. The model finds that the fastest process is thermalization of the hot S_1 excitons with a time constant of $t_1 = 1/k_{th} \approx 44$ fs, in excellent agreement with the empirical fit to the data. The second time scale corresponds to the equilibrium between singlet and triplet excitons with a time constant of $t_2 = 1/k_T \approx 4.4$ ps, also in good agreement with the empirical fit value of ~ 3 ps. The third time scale corresponds to internal conversion with a time constant of $t_3 = 1/k_r \approx 605$ ps. The discrepancy between t_3 and the empirical fit value of ~ 250 ps is likely owing to the fact that the triexponential fit includes an offset, while the kinetic model does not. Regardless, the fits for both of the spots examined in the film fit the data well. Note that we find the fit time scales for physical processes at the orange spot to agree with those at the green spot in a different domain, even though the appearance of their transients at any given polarization is very different. It is likely that these two domains are oriented similarly with respect to the plane of the substrate, though rotated azimuthally from one another. This finding indicates that our drop-cast films likely take on similar domain orientations to the X-ray crystal structure over much of the film area.

The fit to the kinetic model also successfully captures interesting features in the data, and removing any one parameter significantly impairs the fit. For example, in Figure 5a, the amplitude of the fast component in the traces seems to decrease for traces with increasingly positive signal, with the exception of the $\theta_{pr} = 165^\circ$ trace (purple), which has a larger amplitude and faster decay than both of the adjacent traces, and the model captures this result well. The fit accurately captures the polarization dependence of both data sets, as seen in Figure 5c. Additionally, the orientation of the transition dipoles μ_1^o and

μ_1^n were unconstrained in the fit, yet they are found to be perpendicular to the orientation of μ_0 in each domain.

Finally, the model fit also finds that the energetic splitting between the S_1^0 and TT states is 26 meV, with the TT state slightly higher in energy. While the model fitting places the TT state higher in energy than the S_1^0 state, Ramanan et al.¹⁰ find a larger singlet fission yield that would require the TT state to be lower in energy than S_1^0 . This difference could be because of different sample morphologies probed. It is also possible that we have underestimated the triplet yield in our simple model by not including the subsequent correlated triplet separation, $TT \rightarrow T + T$, which would provide a greater driving force for the singlet fission process. Regardless, the minimal energy difference that we obtain indicates that the S_1^0 and TT states are effectively resonant with one another when thermal effects are taken into account and may provide some insight into the degree of resonance between the singlet and triplet pair energies, a property which could be tuned through molecular functionalization and design.

5. CONCLUSIONS

In summary, we have investigated the ultrafast photophysics within individual domains of the small-molecule organic semiconductor TIPS-Pn by focusing laser pulses down to spot sizes 3 orders of magnitude smaller than in more traditional bulk transient absorption measurements. We have used TA signatures as contrast agents to distinguish different ordered domains within the film, and we have also observed a strong polarization dependence in the TA signal on account of the constituent molecules' anisotropy, which would have been averaged in bulk measurements. Thus, we have developed a clear picture of the exciton dynamics occurring in TIPS-Pn films and a kinetic model that is consistent with our subdomain measurements and that can be used successfully in multiple different domains. Our findings suggest that excitation at the band edge leads to population of a hot singlet excited state that vibrationally relaxes on a 50 fs time scale. Subsequently, singlet fission can occur, reaching an equilibrium on a few picoseconds time scale, with exciton recombination following over hundreds of picoseconds. The rapid singlet fission rate makes TIPS-Pn an excellent model system for studying the effects of triplet generation to boost the quantum efficiency of solar cells. The fit of our kinetic model to a data set at any given location in the TIPS-Pn film is constrained far more than would be the case if we were unable to obtain independent transients for multiple light polarizations. The fit provides an estimate of the positioning of the triplet state with respect to the singlet in this material—a parameter that could be tuned in order to optimize device efficiency by molecular functionalization and design.

Though the polarized optical response in different adjacent domains in TIPS-Pn can appear disparate at first glance, we find that the differences can often be reconciled by considering domain orientation. With an understanding of the optical response in individual adjacent domains, it may now be possible to pose and answer further questions about the electronic structure and dynamics at domain boundaries, where significant exciton or charge trapping may occur. In the future, applying similar approaches to investigate these interfaces may shed light on bottlenecks and inefficiencies in organic semiconducting electronics and photovoltaics. In this vein, we also anticipate the utility of TA microscopy for examining more complex film

microstructures, perhaps with the possibility of subdiffraction excitation volumes.

■ ASSOCIATED CONTENT

§ Supporting Information

Fits of TA data to triexponential function; dependence of TA signal on incident pump power; fits of polarization dependence of TA data to sinusoids; fits of TA signal to kinetic model. This material is available free of charge via the Internet at <http://pubs.acs.org>.

■ AUTHOR INFORMATION

Corresponding Author

*E-mail: nsnginsberg@berkeley.edu.

Author Contributions

[†]These authors contributed equally to this work.

Notes

The authors declare no competing financial interest.

■ ACKNOWLEDGMENTS

This work has been supported by the Defense Advanced Research Projects Agency Young Faculty Award number N66001-12-1-4228. C.Y.W. thanks the Natural Sciences and Engineering Research Council, Canada, for a Postdoctoral Fellowship. S.B.P. acknowledges a Department of Energy Office of Science Graduate Research Fellowship, made possible in part by the American Recovery and Reinvestment Act of 2009, administered by ORISE-ORAU under contract no. DE-AC05-06OR23100; B.L.C. acknowledges a National Science Foundation Graduate Research Fellowship (DGE 1106400); R.N. acknowledges the Philomathia Foundation for support; and N.S.G. acknowledges a David and Lucile Packard Foundation Fellowship for Science and Engineering. We also thank V. Ho and R. Segalman for advice in sample preparation.

■ REFERENCES

- (1) Helgesen, M.; Søndergaard, R.; Krebs, F. C. Advanced Materials and Processes for Polymer Solar Cell Devices. *J. Mater. Chem.* **2009**, *20*, 36–60.
- (2) Krebs, F. C. Fabrication and Processing of Polymer Solar Cells: A Review of Printing and Coating Techniques. *Sol. Energy Mater. Sol. Cells* **2009**, *93*, 394–412.
- (3) Günes, S.; Neugebauer, H.; Sariciftci, N. S. Conjugated Polymer-Based Organic Solar Cells. *Chem. Rev.* **2007**, *107*, 1324–1338.
- (4) Kippelen, B.; Brédas, J.-L. Organic Photovoltaics. *Energy Environ. Sci.* **2009**, *2*, 251–261.
- (5) Hoppe, H.; Sariciftci, N. S. Organic Solar Cells: An Overview. *J. Mater. Res.* **2004**, *19*, 1924–1945.
- (6) He, Z.; Zhong, C.; Su, S.; Xu, M.; Wu, H.; Cao, Y. Enhanced Power-conversion Efficiency in Polymer Solar Cells Using an Inverted Device Structure. *Nat. Photonics* **2012**, *6*, 591–595.
- (7) Lanzani, G. Pump Probe and Other Modulation Techniques. In *The Photophysics behind Photovoltaics and Photonics*; Wiley-VCH Verlag GmbH & Co. KGaA: Weinheim, Germany, 2012.
- (8) Megerle, U.; Pugliesi, I.; Schriever, C.; Sailer, C. F.; Riedle, E. Sub-50 fs Broadband Absorption Spectroscopy with Tunable Excitation: Putting the Analysis of Ultrafast Molecular Dynamics on Solid Ground. *Appl. Phys. B: Laser Opt.* **2009**, *96*, 215–231.
- (9) Pollard, W. T.; Mathies, R. A. Analysis of Femtosecond Dynamic Absorption Spectra of Nonstationary States. *Annu. Rev. Phys. Chem.* **1992**, *43*, 497–523.
- (10) Ramanan, C.; Smeigh, A. L.; Anthony, J. E.; Marks, T. J.; Wasielewski, M. R. Competition Between Singlet Fission and Charge Separation in Solution-Processed Blend Films of 6,13-Bis-(triisopropylsilyl)ethynylpentacene with Sterically-Encumbered Per-

ylene-3,4:9,10-bis(dicarboximide)s. *J. Am. Chem. Soc.* **2012**, *134*, 386–397.

(11) Rao, A.; Wilson, M. W. B.; Albert-Seifried, S.; Di Pietro, R.; Friend, R. H. Photophysics of Pentacene Thin Films: The Role of Exciton Fission and Heating Effects. *Phys. Rev. B* **2011**, *84*, 195411.

(12) Thorsmølle, V. K.; Averitt, R. D.; Demsar, J.; Smith, D. L.; Tretiak, S.; Martin, R. L.; Chi, X.; Crone, B. K.; Ramirez, A. P.; Taylor, A. J. Photoexcited Carrier Relaxation Dynamics in Pentacene Probed by Ultrafast Optical Spectroscopy: Influence of Morphology on Relaxation Processes. *Phys. B Condens. Matter* **2009**, *404*, 3127–3130.

(13) Wilson, M. W. B.; Rao, A.; Clark, J.; Kumar, R. S. S.; Brida, D.; Cerullo, G.; Friend, R. H. Ultrafast Dynamics of Exciton Fission in Polycrystalline Pentacene. *J. Am. Chem. Soc.* **2011**, *133*, 11830–11833.

(14) Chen, J.; Tee, C. K.; Shtein, M.; Anthony, J.; Martin, D. C. Grain-boundary-limited Charge Transport in Solution-processed 6,13 Bis(triisopropylsilyl)ethynyl Pentacene Thin Film Transistors. *J. Appl. Phys.* **2008**, *103*, 114513.

(15) Rivnay, J.; Jimison, L. H.; Northrup, J. E.; Toney, M. F.; Noriega, R.; Lu, S.; Marks, T. J.; Facchetti, A.; Salleo, A. Large Modulation of Carrier Transport by Grain-boundary Molecular Packing and Microstructure in Organic Thin Films. *Nat. Mater.* **2009**, *8*, 952–958.

(16) he doeMarsh, R. A.; Groves, C.; Greenham, N. C. A Microscopic Model for the Behavior of Nanostructured Organic Photovoltaic Devices. *J. Appl. Phys.* **2007**, *101*, 083509.

(17) Chen, J.; Martin, D. C.; Anthony, J. E. Morphology and Molecular Orientation of Thin-film Bis(triisopropylsilyl)ethynyl Pentacene. *J. Mater. Res.* **2007**, *22*, 1701–1709.

(18) Dickey, K. C.; Anthony, J. E.; Loo, Y.-L. Improving Organic Thin-Film Transistor Performance through Solvent-Vapor Annealing of Solution-Processable Triethylsilyl ethynyl Anthradithiophene. *Adv. Mater.* **2006**, *18*, 1721–1726.

(19) Shi, Y.; Liu, J.; Yang, Y. Device Performance and Polymer Morphology in Polymer Light Emitting Diodes: The Control of Thin Film Morphology and Device Quantum Efficiency. *J. Appl. Phys.* **2000**, *87*, 4254–4263.

(20) Yin, W.; Dadmun, M. A New Model for the Morphology of P3HT/PCBM Organic Photovoltaics from Small-Angle Neutron Scattering: Rivers and Streams. *ACS Nano* **2011**, *5*, 4756–4768.

(21) Chen, D.; Nakahara, A.; Wei, D.; Nordlund, D.; Russell, T. P. P3HT/PCBM Bulk Heterojunction Organic Photovoltaics: Correlating Efficiency and Morphology. *Nano Lett.* **2011**, *11*, 561–567.

(22) Verploegen, E.; Miller, C. E.; Schmidt, K.; Bao, Z.; Toney, M. F. Manipulating the Morphology of P3HT–PCBM Bulk Heterojunction Blends with Solvent Vapor Annealing. *Chem. Mater.* **2012**, *24*, 3923–3931.

(23) Ruderer, M. A.; Müller-Buschbaum, P. Morphology of Polymer-based Bulk Heterojunction Films for Organic Photovoltaics. *Soft Matter* **2011**, *7*, 5482–5493.

(24) Rivnay, J.; Noriega, R.; Kline, R. J.; Salleo, A.; Toney, M. F. Quantitative Analysis of Lattice Disorder and Crystallite Size in Organic Semiconductor Thin Films. *Phys. Rev. B* **2011**, *84*, 045203.

(25) Hoppe, H.; Sariciftci, N. S. Morphology of Polymer/fullerene Bulk Heterojunction Solar Cells. *J. Mater. Chem.* **2006**, *16*, 45–61.

(26) Giri, G.; Verploegen, E.; Mannsfeld, S. C. B.; Atahan-Evrenk, S.; Kim, D. H.; Lee, S. Y.; Becerril, H. A.; Aspuru-Guzik, A.; Toney, M. F.; Bao, Z. Tuning Charge Transport in Solution-sheared Organic Semiconductors Using Lattice Strain. *Nature* **2011**, *480*, 504–508.

(27) Stingelin-Stutzmann, N.; Smits, E.; Wondereg, H.; Tanase, C.; Blom, P.; Smith, P.; de Leeuw, D. Organic Thin-film Electronics from Vitreous Solution-processed Rubrene Hypereutectics. *Nat. Mater.* **2005**, *4*, 601–606.

(28) Minari, T.; Kano, M.; Miyadera, T.; Wang, S.-D.; Aoyagi, Y.; Seto, M.; Nemoto, T.; Isoda, S.; Tsukagoshi, K. Selective Organization of Solution-processed Organic Field-effect Transistors. *Appl. Phys. Lett.* **2008**, *92*, 173301.

(29) Sun, Y.; Liu, Y.; Zhu, D. Advances in Organic Field-effect Transistors. *J. Mater. Chem.* **2005**, *15*, 53.

(30) Treat, N. D.; Nekuda Malik, J. A.; Reid, O.; Yu, L.; Shuttle, C. G.; Rumbles, G.; Hawker, C. J.; Chabinyc, M. L.; Smith, P.; Stingelin, N. Microstructure Formation in Molecular and Polymer Semiconductors Assisted by Nucleation Agents. *Nat. Mater.* **2013**, *12*, 628–633.

(31) Min, W.; Freudiger, C. W.; Lu, S.; Xie, X. S. Coherent Nonlinear Optical Imaging: Beyond Fluorescence Microscopy. *Annu. Rev. Phys. Chem.* **2011**, *62*, 507–530.

(32) Min, W.; Lu, S.; Chong, S.; Roy, R.; Holtom, G. R.; Xie, X. S. Imaging Chromophores with Undetectable Fluorescence by Stimulated Emission Microscopy. *Nature* **2009**, *461*, 1105–1109.

(33) Fu, D.; Ye, T.; Yurtsever, G.; Warren, W. S.; Matthews, T. E. Two-color, Two-photon, and Excited-state Absorption Microscopy. *J. Biomed. Opt.* **2007**, *12*, 054004.

(34) Ye, T.; Fu, D.; Warren, W. S. Nonlinear Absorption Microscopy. *Photochem. Photobiol.* **2009**, *85*, 631–645.

(35) Matthews, T. E.; Piletic, I. R.; Selim, M. A.; Simpson, M. J.; Warren, W. S. Pump-Probe Imaging Differentiates Melanoma from Melanocytic Nevi. *Sci. Transl. Med.* **2011**, *3*, 71ra15.

(36) Carey, C. R.; LeBel, T.; Crisostomo, D.; Giblin, J.; Kuno, M.; Hartland, G. V. Imaging and Absolute Extinction Cross-Section Measurements of Nanorods and Nanowires through Polarization Modulation Microscopy. *J. Phys. Chem. C* **2010**, *114*, 16029–16036.

(37) Hartland, G. V. Ultrafast Studies of Single Semiconductor and Metal Nanostructures through Transient Absorption Microscopy. *Chem. Sci.* **2010**, *1*, 303–309.

(38) Staleva, H.; Hartland, G. V. Vibrational Dynamics of Silver Nanocubes and Nanowires Studied by Single-Particle Transient Absorption Spectroscopy. *Adv. Funct. Mater.* **2008**, *18*, 3809–3817.

(39) Staleva, H.; Skrabalak, S. E.; Carey, C. R.; Kosel, T.; Xia, Y.; Hartland, G. V. Coupling to Light, and Transport and Dissipation of Energy in Silver Nanowires. *Phys. Chem. Chem. Phys.* **2009**, *11*, 5889–5896.

(40) Huang, L.; Cheng, J.-X. Nonlinear Optical Microscopy of Single Nanostructures. *Annu. Rev. Mater. Res.* **2013**, *43*, 213–236.

(41) Gabriel, M. M.; Kirschbrown, J. R.; Christesen, J. D.; Pinion, C. W.; Zigler, D. F.; Grumstrup, E. M.; Mehl, B. P.; Cating, E. E. M.; Cahoon, J. F.; Papanikolas, J. M. Direct Imaging of Free Carrier and Trap Carrier Motion in Silicon Nanowires by Spatially-Separated Femtosecond Pump–Probe Microscopy. *Nano Lett.* **2013**, *13*, 1336–1340.

(42) Mehl, B. P.; Kirschbrown, J. R.; House, R. L.; Papanikolas, J. M. The End Is Different Than The Middle: Spatially Dependent Dynamics in ZnO Rods Observed by Femtosecond Pump–Probe Microscopy. *J. Phys. Chem. Lett.* **2011**, *2*, 1777–1781.

(43) Wang, P.; Slipchenko, M. N.; Mitchell, J.; Yang, C.; Potma, E. O.; Xu, X.; Cheng, J.-X. Far-field Imaging of Non-fluorescent Species with Subdiffraction Resolution. *Nat. Photonics* **2013**, *7*, 449–453.

(44) Gao, B.; Hartland, G.; Fang, T.; Kelly, M.; Jena, D.; Xing, H.; Huang, L. Studies of Intrinsic Hot Phonon Dynamics in Suspended Graphene by Transient Absorption Microscopy. *Nano Lett.* **2011**, *11*, 3184–3189.

(45) Huang, L.; Hartland, G. V.; Chu, L.-Q.; Luxmi; Feenstra, R. M.; Lian, C.; Tahy, K.; Xing, H. Ultrafast Transient Absorption Microscopy Studies of Carrier Dynamics in Epitaxial Graphene. *Nano Lett.* **2010**, *10*, 1308–1313.

(46) Ruzicka, B. A.; Wang, S.; Liu, J.; Loh, K.-P.; Wu, J. Z.; Zhao, H. Spatially Resolved Pump-probe Study of Single-layer Graphene Produced by Chemical Vapor Deposition. *Opt. Mater. Express* **2012**, *2*, 708–716.

(47) Grancini, G.; Martino, N.; Bianchi, M.; Rizzi, L. G.; Russo, V.; Li Bassi, A.; Casari, C. S.; Petrozza, A.; Sordan, R.; Lanzani, G. Ultrafast Spectroscopic Imaging of Exfoliated Graphene. *Phys. Status Solidi B* **2012**, *249*, 2497–2499.

(48) Tamai, N.; Porter, C. F.; Masuhara, H. Femtosecond Transient Absorption Spectroscopy of a Single Perylene Microcrystal Under a Microscope. *Chem. Phys. Lett.* **1993**, *211*, 364–370.

(49) Yago, T.; Tamaki, Y.; Furube, A.; Katoh, R. Self-trapping Limited Exciton Diffusion in a Monomeric Perylene Crystal as

Revealed by Femtosecond Transient Absorption Microscopy. *Phys. Chem. Chem. Phys.* **2008**, *10*, 4435–4441.

(50) Matsuda, H.; Fujimoto, Y.; Ito, S.; Nagasawa, Y.; Miyasaka, H.; Asahi, T.; Masuhara, H. Development of Near-Infrared 35 fs Laser Microscope and Its Application to the Detection of Three- and Four-Photon Fluorescence of Organic Microcrystals. *J. Phys. Chem. B* **2006**, *110*, 1091–1094.

(51) Cabanillas-Gonzalez, J.; Grancini, G.; Lanzani, G. Pump-Probe Spectroscopy in Organic Semiconductors: Monitoring Fundamental Processes of Relevance in Optoelectronics. *Adv. Mater.* **2011**, *23*, 5468–5485.

(52) Grancini, G.; Polli, D.; Fazzi, D.; Cabanillas-Gonzalez, J.; Cerullo, G.; Lanzani, G. Transient Absorption Imaging of P3HT:PCBM Photovoltaic Blend: Evidence For Interfacial Charge Transfer State. *J. Phys. Chem. Lett.* **2011**, *2*, 1099–1105.

(53) Polli, D.; Grancini, G.; Clark, J.; Celebrano, M.; Virgili, T.; Cerullo, G.; Lanzani, G. Nanoscale Imaging of the Interface Dynamics in Polymer Blends by Femtosecond Pump-Probe Confocal Microscopy. *Adv. Mater.* **2010**, *22*, 3048–3051.

(54) Virgili, T.; Grancini, G.; Molotokaite, E.; Suarez-Lopez, I.; Rajendran, S. K.; Liscio, A.; Palermo, V.; Lanzani, G.; Polli, D.; Cerullo, G. Confocal Ultrafast Pump-probe Spectroscopy: a New Technique to Explore Nanoscale Composites. *Nanoscale* **2012**, *4*, 2219–2226.

(55) Wong, C. T. O.; Lo, S. S.; Huang, L. Ultrafast Spatial Imaging of Charge Dynamics in Heterogeneous Polymer Blends. *J. Phys. Chem. Lett.* **2012**, *3*, 879–884.

(56) Pope, M.; Swenberg, C. E. *Electronic Processes in Organic Crystals and Polymers*, 2nd ed.; Oxford University Press: Oxford, UK, 1999.

(57) Birks, J. B. *Photophysics of Aromatic Molecules*; Wiley: New York, 1970.

(58) McGlynn, S. P.; Azumi, T. *Molecular Spectroscopy of the Triplet State*; Prentice-Hall Inc.: Englewood Cliffs, NJ, 1969.

(59) Kleven, H. B.; Platt, J. R. Spectral Resemblances of Cata-Condensed Hydrocarbons. *J. Chem. Phys.* **1949**, *17*, 470–481.

(60) Platt, J. R. Classification of Spectra of Cata-Condensed Hydrocarbons. *J. Chem. Phys.* **1949**, *17*, 484–495.

(61) Anthony, J. E. Functionalized Acenes and Heteroacenes for Organic Electronics. *Chem. Rev.* **2006**, *106*, 5028–5048.

(62) Lloyd, M. T.; Anthony, J. E.; Malliaras, G. G. Photovoltaics from Soluble Small Molecules. *Mater. Today* **2007**, *10*, 34–41.

(63) Anthony, J. E. The Larger Acenes: Versatile Organic Semiconductors. *Angew. Chem., Int. Ed.* **2008**, *47*, 452–483.

(64) West, B. A.; Womick, J. M.; McNeil, L. E.; Tan, K. J.; Moran, A. M. Ultrafast Dynamics of Frenkel Excitons in Tetracene and Rubrene Single Crystals. *J. Phys. Chem. C* **2010**, *114*, 10580–10591.

(65) Roberts, S. T.; McAnally, R. E.; Mastron, J. N.; Webber, D. H.; Whited, M. T.; Brutchey, R. L.; Thompson, M. E.; Bradforth, S. E. Efficient Singlet Fission Discovered in a Disordered Acene Film. *J. Am. Chem. Soc.* **2012**, *134*, 6388–6400.

(66) Bardeen, C. J. Excitonic Processes in Molecular Crystalline Materials. *MRS Bull.* **2013**, *38*, 65–71.

(67) Congreve, D. N.; Lee, J.; Thompson, N. J.; Hontz, E.; Yost, S. R.; Reusswig, P. D.; Bahlke, M. E.; Reineke, S.; Voorhis, T. V.; Baldo, M. A. External Quantum Efficiency Above 100% in a Singlet-Exciton-Fission-Based Organic Photovoltaic Cell. *Science* **2013**, *340*, 334–337.

(68) Lee, J.; Jadhav, P.; Reusswig, P. D.; Yost, S. R.; Thompson, N. J.; Congreve, D. N.; Hontz, E.; Van Voorhis, T.; Baldo, M. A. Singlet Exciton Fission Photovoltaics. *Acc. Chem. Res.* **2013**, *46*, 1300–1311.

(69) Anthony, J. E.; Brooks, J. S.; Eaton, D. L.; Parkin, S. R. Functionalized Pentacene: Improved Electronic Properties from Control of Solid-State Order. *J. Am. Chem. Soc.* **2001**, *123*, 9482–9483.

(70) Sheraw, C. D.; Jackson, T. N.; Eaton, D. L.; Anthony, J. E. Functionalized Pentacene Active Layer Organic Thin-Film Transistors. *Adv. Mater.* **2003**, *15*, 2009–2011.

(71) Griffith, O. L.; Anthony, J. E.; Jones, A. G.; Lichtenberger, D. L. Electronic Properties of Pentacene Versus Triisopropylsilyl-Substituted Pentacene: Environment-Dependent Effects of the Silyl Substituent. *J. Am. Chem. Soc.* **2010**, *132*, 580–586.

(72) Lloyd, M. T.; Mayer, A. C.; Tayi, A. S.; Bowen, A. M.; Kasen, T. G.; Herman, D. J.; Mourey, D. A.; Anthony, J. E.; Malliaras, G. G. Photovoltaic Cells from a Soluble Pentacene Derivative. *Org. Electron.* **2006**, *7*, 243–248.

(73) Palilis, L. C.; Lane, P. A.; Kushto, G. P.; Purushothaman, B.; Anthony, J. E.; Kafafi, Z. H. Organic Photovoltaic Cells with High Open Circuit Voltages Based on Pentacene Derivatives. *Org. Electron.* **2008**, *9*, 747–752.

(74) Ostroverkhova, O.; Shcherbyna, S.; Cooke, D. G.; Egerton, R. F.; Hegmann, F. A.; Tykewinski, R. R.; Parkin, S. R.; Anthony, J. E. Optical and Transient Photoconductive Properties of Pentacene and Functionalized Pentacene Thin Films: Dependence on Film Morphology. *J. Appl. Phys.* **2005**, *98*, 033701.

(75) Ostroverkhova, O.; Cooke, D. G.; Shcherbyna, S.; Egerton, R. F.; Hegmann, F. A.; Tykewinski, R. R.; Anthony, J. E. Bandlike Transport in Pentacene and Functionalized Pentacene Thin Films Revealed by Subpicosecond Transient Photoconductivity Measurements. *Phys. Rev. B* **2005**, *71*, 035204.

(76) Ostroverkhova, O.; Cooke, D. G.; Hegmann, F. A.; Anthony, J. E.; Podzorov, V.; Gershenson, M. E.; Jurchescu, O. D.; Palstra, T. T. M. Ultrafast Carrier Dynamics in Pentacene, Functionalized Pentacene, Tetracene, and Rubrene Single Crystals. *Appl. Phys. Lett.* **2006**, *88*, 162101.

(77) Mannsfeld, S. C. B.; Tang, M. L.; Bao, Z. Thin Film Structure of Triisopropylsilyl-ethynyl-Functionalized Pentacene and Tetracene[2,3-b]thiophene from Grazing Incidence X-Ray Diffraction. *Adv. Mater.* **2011**, *23*, 127–131.

(78) Maliakal, A.; Raghavachari, K.; Katz, H.; Chandross, E.; Siegrist, T. Photochemical Stability of Pentacene and a Substituted Pentacene in Solution and in Thin Films. *Chem. Mater.* **2004**, *16*, 4980–4986.

(79) Platt, A. D.; Day, J.; Subramanian, S.; Anthony, J. E.; Ostroverkhova, O. Optical, Fluorescent, and (Photo)conductive Properties of High-Performance Functionalized Pentacene and Anthradithiophene Derivatives. *J. Phys. Chem. C* **2009**, *113*, 14006–14014.

(80) Gélinas, S.; Kirkpatrick, J.; Howard, I. A.; Johnson, K.; Wilson, M. W. B.; Pace, G.; Friend, R. H.; Silva, C. Recombination Dynamics of Charge Pairs in a Push–Pull Polyfluorene-Derivative. *J. Phys. Chem. B* **2013**, *117*, 4649–4653.

(81) Xu, Q.-H.; Moses, D.; Heeger, A. J. Direct Observation of a Time-delayed Intermediate State Generated via Exciton-exciton Annihilation in Polyfluorene. *Phys. Rev. B* **2003**, *68*, 174303.

(82) Kaake, L. G.; Moses, D.; Heeger, A. J. Coherence and Uncertainty in Nanostructured Organic Photovoltaics. *J. Phys. Chem. Lett.* **2013**, *4*, 2264–2268.

(83) Kaake, L. G.; Jasieniak, J. J.; Bakus, R. C.; Welch, G. C.; Moses, D.; Bazan, G. C.; Heeger, A. J. Photoinduced Charge Generation in a Molecular Bulk Heterojunction Material. *J. Am. Chem. Soc.* **2012**, *134*, 19828–19838.

(84) Jailaubekov, A. E.; Willard, A. P.; Tritsch, J. R.; Chan, W.-L.; Sai, N.; Gearba, R.; Kaake, L. G.; Williams, K. J.; Leung, K.; Rossky, P. J.; et al. Hot Charge-transfer Excitons Set the Time Limit for Charge Separation at Donor/acceptor Interfaces in Organic Photovoltaics. *Nat. Mater.* **2013**, *12*, 66–73.

(85) Grancini, G.; Maiuri, M.; Fazzi, D.; Petrozza, A.; Egelhaaf, H.-J.; Brida, D.; Cerullo, G.; Lanzani, G. Hot Exciton Dissociation in Polymer Solar Cells. *Nat. Mater.* **2013**, *12*, 29–33.

(86) Bakulin, A. A.; Rao, A.; Pavelyev, V. G.; van Loosdrecht, P. H. M.; Pshenichnikov, M. S.; Niedzialek, D.; Cornil, J.; Beljonne, D.; Friend, R. H. The Role of Driving Energy and Delocalized States for Charge Separation in Organic Semiconductors. *Science* **2012**, *335*, 1340–1344.

(87) Clarke, T. M.; Durrant, J. R. Charge Photogeneration in Organic Solar Cells. *Chem. Rev.* **2010**, *110*, 6736–6767.

(88) Banerji, N. Sub-picosecond Delocalization in the Excited State of Conjugated Homopolymers and Donor–acceptor Copolymers. *J. Mater. Chem. C* **2013**, *1*, 3052–3066.

(89) Lee, J.; Vandewal, K.; Yost, S. R.; Bahlke, M. E.; Goris, L.; Baldo, M. A.; Manca, J. V.; Voorhis, T. V. Charge Transfer State Versus Hot

Exciton Dissociation in Polymer–Fullerene Blended Solar Cells. *J. Am. Chem. Soc.* **2010**, *132*, 11878–11880.

(90) Burkhard, G. F.; Hoke, E. T.; Beiley, Z. M.; McGehee, M. D. Free Carrier Generation in Fullerene Acceptors and Its Effect on Polymer Photovoltaics. *J. Phys. Chem. C* **2012**, *116*, 26674–26678.

(91) Smith, M. B.; Michl, J. Recent Advances in Singlet Fission. *Annu. Rev. Phys. Chem.* **2013**, *64*, 361–386.